



## A Fiber Optic Distributed Temperature Sensor for Continuous *in situ* Profiling 2 km Beneath Constant-altitude Scientific Balloons

5 J. Douglas Goetz<sup>1</sup>, Lars K. Kalnajs<sup>1</sup>, Terry Deshler<sup>1</sup>, Sean Davis<sup>2</sup>, Martina Bramberger<sup>3</sup>, M. Joan Alexander<sup>3</sup>

[1] Laboratory for Atmospheric and Space Physics, University of Colorado at Boulder, Boulder, CO, USA

[2] NOAA Chemical Sciences Laboratory, Boulder, CO, USA

[3] NorthWest Research Associates, CoRA Office, Boulder, Colorado, USA

10

*Correspondence to:* J. Douglas Goetz (doug.goetz@lasp.colorado.edu)

**Abstract.** A novel fiber optic distributed temperature sensing instrument named the Fiber-optic Laser Operated Atmospheric Temperature Sensor, or FLOATS, was developed for continuous *in situ* profiling of the atmosphere up to 2 km below constant altitude scientific balloons. The temperature sensing system uses a suspended fiber optic cable and temperature dependent scattering of pulsed laser light in the Raman regime to retrieve continuous 3 m vertical resolution profiles at a minimum sampling period of 20 s. FLOATS was designed for operation aboard drifting superpressure balloons in the tropical tropopause layer at altitudes around 18 km as part of the Stratéole 2 campaign. A short test flight of the system was conducted from Laramie, Wyoming, in January 2021 to check the optical, electrical, and mechanical systems at altitude and to validate a four-reference temperature calibration procedure with a fiber optic deployment length of 1170 m. During the 4-hour flight aboard a vented balloon, FLOATS retrieved temperature profiles during ascent and while at a constant float altitude of about 19 km. The FLOATS retrievals provided differences of less than 1.0°C compared to a commercial radiosonde aboard the flight payload during ascent. At float altitude, a comparison of optical length and GPS position at the bottom of the fiber optic revealed little to no curvature in the fiber optic cable suggesting that the position of any distributed temperature measurement can be effectively modeled. Comparisons of the distributed temperature retrievals to the reference temperature sensors show strong agreement with root mean square error values less than 0.4°C. The instrument also demonstrated good agreement with nearby meteorological observations and COSMIC-2 satellite profiles. Observations of temperature and wind perturbations compared to the nearby radiosounding profiles provide evidence of inertial gravity wave activity during the test flight. Spectral analysis of the observed temperature perturbations shows that FLOATS is an effective and pioneering tool for the investigation of small scale gravity waves in the lower stratosphere.

15  
20  
25  
30

35



## 1 Introduction

Distributed temperature sensing (DTS) uses fiber optic cable to obtain continuous profiles of temperature along the length of the fiber at a high time resolution. The sensing method is distinct from single point fiber optic techniques like fiber Bragg gratings in that it uses temperature dependent light scattering in the Rayleigh, Brillouin, or Raman regimes within the fiber optic core in conjunction with optical time domain reflectometry to acquire uninterrupted temperature along the longitudinal axis (Lu et al., 2019). Raman spectra DTS has gained popularity within the earth sciences because it is a lower cost and simple method for measuring temperature in harsh environments and for sensing temperature gradients over large spatial domains relative to pointwise sensors (Tyler et al., 2009). Applications of DTS in environmental sensing have largely been centered around hydrologic and geologic research (Drusová et al., 2021; Henniges and Masoudi, 2021; Lagos et al., 2020; Selker et al., 2006; Sinnett et al., 2020; Tyler et al., 2009), but there has been increased interest in using DTS for atmospheric measurements over the last decade. Past atmospheric measurements with DTS can generally be categorized into three fields including surface layer to air interactions (Peltola et al., 2021; Petrides et al., 2011; Thomas et al., 2012), boundary layer dynamics (Egerer et al., 2019; Higgins et al., 2018; Keller et al., 2011), and wind measurements (Sayde et al., 2015; van Ramshorst et al., 2020). In two aerial studies, including measurements aboard a tethered balloon (Keller et al., 2011) and aboard an unmanned aircraft (Higgins et al., 2018), Raman spectra DTS was found to be reliable compared to traditional temperature sensors.

Here we present a novel balloon-borne DTS system for atmospheric temperature profiling of up to 2 km within the upper troposphere and lower stratosphere (UTLS). The UTLS is a globally important region of the atmosphere defined by its thermal structure, with a positive lapse rate in the troposphere terminated at a cold point and a subsequent shift to a negative lapse rate in the stratosphere. Temperature structure within the UTLS plays a role in the transport and chemistry of trace gases and aerosol. In the tropics, for example, stratospheric water vapor concentrations are controlled by the thermal structure of the Tropical Tropopause Layer (TTL; Chang and L'Ecuyer, 2020; Fueglistaler et al., 2009; Randel and Jensen, 2013). Routine temperature measurements in this region are made by satellite sensors and a sparse network of equatorial radiosondes. Current space-based temperature measurements made by Global Navigation Satellite System (GNSS) radio occultation (GNSS-RO; e.g. COSMIC-2) or nadir sounding (e.g. AMSU) provide near-global coverage making them ideal for broad climate studies (Khaykin et al., 2017). However, nadir sounding measurements have limited vertical resolution and are limited in their diurnal sampling, whereas GNSS-RO systems have highly variable spatial coverage. Both systems have horizontal resolutions ranging from a few kilometers to hundreds of kilometers. Balloon-borne radio soundings of atmospheric temperature are



performed on a regular basis at numerous locations as they are part of the daily observations used for aviation and meteorology. Radiosonde temperature measurements provide high vertical resolution (5 - 100 m), over  
70 a large altitude range (~0-30 km), but only retrieve one vertical profile per flight and have low temporal resolution as they are typically performed once or twice per day. Thus, neither technique is ideal for investigating small scale thermal structure and its evolution over space and time, such as may occur due to gravity waves. The instrument described here overcomes both these limitations by collecting near-continuous, 3 m vertical resolution temperature measurements through the vertical extent of the UTLS.

75 To investigate the thermal structure of the UTLS the novel Fiber-optic Laser Operated Atmospheric Temperature Sensor (FLOATS) instrument was developed. The conception of the instrument was motivated by Stratéole 2, an international mission, which aims to investigate dynamics, transport, and chemistry within the TTL and tropical lower stratosphere using constant density balloons with flight durations up to 4 months (Haase et al., 2018). The FLOATS instrument was deployed on two long-duration balloon flights during the  
80 2021 Stratéole 2 campaign. In this work, however, we describe results from a shorter duration constant altitude mid-latitude flight of the FLOATS instrument that was performed to validate the instrument for the Stratéole 2 mission. Temperature calibration and analysis techniques validated with the mid-latitude flight provide the necessary proof of concept for the long-duration flights and demonstrate that DTS is an effective tool for vertical profiling of the UTLS.

85

## 2 Design and Methods

### 2.1 Instrument Overview

FLOATS is a DTS system that deploys up to 2000 m of fiber optic cable, unreeled from an internal spool, below a high-altitude balloon gondola to obtain temperature profiles at 3 m vertical resolution with a  
90 minimum sampling period of 20 s. The instrument is comprised of three major components including a DTS, mechanical reeling system, and an end of fiber unit (EFU) sub-gondola (Fig 1a). These components were developed for deployment aboard high altitude balloons during the Stratéole 2 mission and are therefore designed to withstand harsh environmental conditions, run semi-autonomously with limited supervision from the ground, and to meet the low power, low mass, and regulatory requirements of high altitude ballooning.  
95 FLOATS was built to meet the requirements for a multi-month flight aboard a Centre national d'études spatiales (CNES) superpressure balloon at a pressure level near 70 hPa, approximately 18km, in the TTL, at latitudes between 15°N and 20°S. This region of the atmosphere is one of the coldest regions below the mesosphere, mean temperatures < -75°C (Fueglistaler et al., 2009)

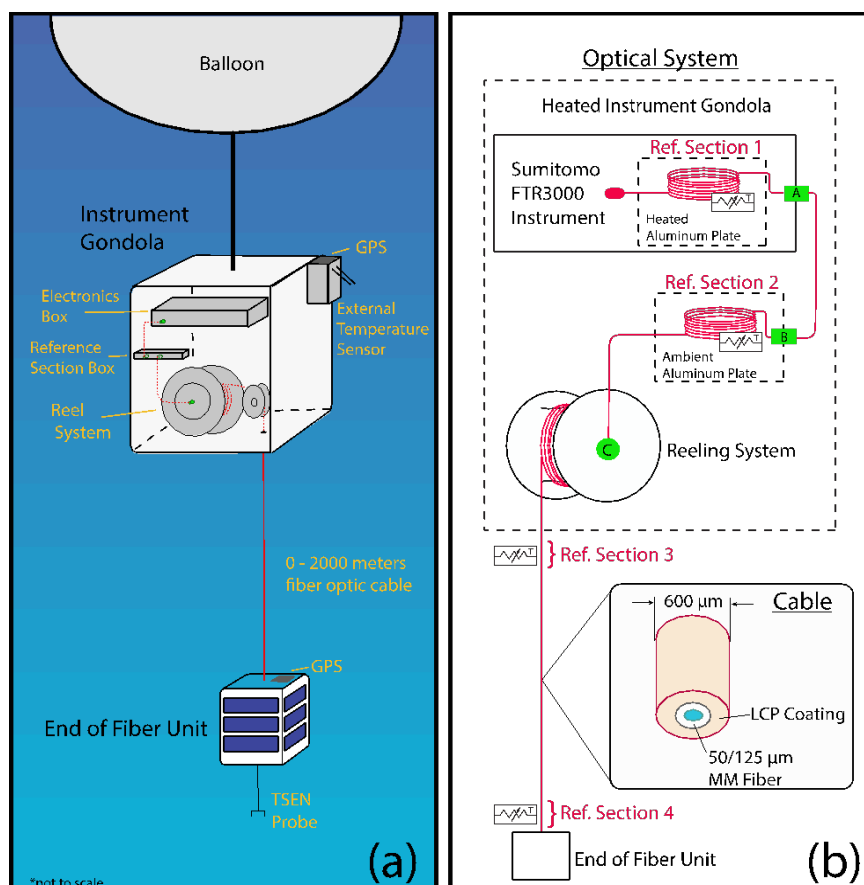


100

105

110

115



120

**Figure 1:** Illustration of the components of the FLOATS instrument (a) and optical system (b). Fiber optic connections are depicted in panel b with green icons. The thermistor electrical symbols depicted in panel b are used to represent the location of a reference temperature sensor.

## 2.2 Optical System

The optical system of FLOATS, illustrated in Figure 1b, is comprised of a commercial DTS optical bench, modified for high altitude operation, control electronics, reinforced multimode fiber optic cable, coiled sections of fiber optic cable at uniform temperature, and reference temperature sensors. The sections of fiber optic cable at uniform temperature combined with reference temperature sensors are identified as Ref. Section X in Figure 1 and RSX in the text, where X is the reference section number. All of the components with the exception of the fiber optic cable when deployed for measurements, are contained within a temperature-controlled balloon gondola ( $-30^{\circ}\text{C} - 30^{\circ}\text{C}$ ). The commercial optical bench is a Sumitomo Electric Industries, Ltd, FTR3000 instrument. The FTR3000 pulses 785 nm Class 1 laser light through the fiber optic cable and

130



senses the Stokes and anti-Stokes scattering at 760 nm and 810 nm, respectively, as a function of time using optical time domain reflectometry. For temperature calibration, the instrument contains a 25 m length of coiled unbuffered fiber laid on a temperature-controlled aluminum plate and immersed in a semi-solid gel (RS1). The FTR3000 with the factory single point calibration system and a ~1 minute sample integration time has a manufacturer specified temperature accuracy of  $\pm 0.7^\circ\text{C}$  at 500 m distance along the fiber,  $\pm 1.0^\circ\text{C}$  at 1000 m, and  $\pm 2.0^\circ\text{C}$  at 2000 m. The manufacturer reports a spatial resolution of 3 m defined as the distance between the 10<sup>th</sup> and 90<sup>th</sup> percentile of the temperature step change.

In FLOATS, the FTR3000 is connected to a second 30 m section of unbuffered multimode fiber optic cable coiled upon a 100 x 100 x 0.81 mm aluminum plate and overlaid with self-leveling silicone adhesive with imbedded temperature sensors all held within an ABS plastic box (RS2 in Fig 1b). The coil is then connected to a fiber optic rotary joint (Princtel, Inc; RFCX-850-50) coupled to the reel system spool which is in turn connected to up to 2000 m of deployable multimode fiber optic cable.

The fiber optic cable used for ambient temperature sensing outside of the balloon gondola is size 50/125  $\mu\text{m}$  multimode fiber optic coated in a proprietary linear crystal polymer (LCP) manufactured by Linden Photonics, Inc for a total diameter of  $600\pm 40\ \mu\text{m}$  (Fig. 1b). The 600  $\mu\text{m}$  diameter LCP fiber optic was chosen to provide a minimum breaking strain of 140 N to meet CNES safety standards and a maximum breaking strain of 230 N for the EFU sub-gondola to be classified as a ‘light balloon’ by ICAO regulatory standards (i.e. Rules of the Air ICAO Appendix 4 Annex 2). The LCP coated fiber optic was also chosen because it exhibits low breaking strain degradation with 90-day equivalent exposure to stratospheric level ultraviolet (UV) light.

The end of fiber optic cable is attached mechanically, but not optically to the EFU sub-gondola. Optical unions between sections of the fiber are component specific and referencing Figure 1b include: A, E2000-APC for the connection of FTR3000 to short patch cord; B, FC-APC for the patch cord to RS2 connection; C, FC-PC for the reference section to rotary joint to spooled cable assembly. Reference temperature sensors (i.e. 10 k ohm NTC thermistors and 100-ohm platinum RTD sensors) are placed on the aluminum plates of RS1 and RS2 for the temperature calibration procedures, which is discussed in Sect. 2.5.

### 2.3 Reeling System

The mechanical reeling system is designed to deploy the spooled fiber optic cable during flight and retract the fiber optic cable at the end of flight. The system consists of a laser sintered carbon-fiber reinforced nylon spool driven by a brushless DC servomotor, planetary gearhead, and electromagnetic brake combination, a stepper motor driven ‘level-wind’ carriage assembly, nylon redirect pulleys, and an electrical



control system. The reeling system is functionally and mechanically similar to the system used by the balloon-  
borne water vapor, cloud, and temperature reel-down instrument RACHuTS fully described in (Kalnajs et  
165 al., 2021), with some minor differences. The DC servomotor assembly, for example, is rated for lower loads  
compared to the RACHuTS instrument (i.e. maximum design load of 19 N vs 35 N) to meet differing mass  
requirements. Additionally, a larger spool diameter (12 cm) and wider bend radius pulleys for redirection of  
the cable compared to RACHuTS were chosen to minimize optical losses attributed to bends in the fiber optic  
170 cable (Zeidler et al., 1976). The reeling system is capable of performing multiple deployments and retractions  
of the entire length of fiber, or variable lengths and variable speeds depending on flight requirements. Typical  
deployment/retraction speeds are between 0.4 m/s and 0.5 m/s and the system has a maximum speed of  
approximately 0.65 m/s. Therefore, for a flight in which 2000 m of fiber optic is required, it will take about  
1 hour to reach full deployment. It should be noted that at least 50 m of fiber optic remains spooled on the  
175 reeling system at any point, to act as a friction anchor and prevent the loss of the cable and end of fiber unit  
while in flight.

#### 2.4 End of Fiber Unit

The end of fiber unit is a 700 gram self-contained sub-gondola used to acquire GPS position, ambient  
180 temperature, and pressure at the end of the FLOATS fiber optic cable. The exterior of the EFU is a box made  
of extruded polystyrene foam with the dimensions of 12.5 cm x 12.5 cm x 20 cm. The fiber optic cable is  
secured to the internal hollow tube frame of the EFU. The closest 10 m of fiber optic to the EFU are reinforced  
with a hollow core Ultra High Molecular Weight Polyethylene (UHMWPE) braid with a breaking strain in  
excess of 400 N for dynamic shock load protection during the launch of FLOATS at which point only the  
185 reinforced section is exposed to the load from the EFU. The interior is insulated with Cabot Thermal Wrap  
silica aerogel blankets and temperature controlled to  $-5^{\circ}\text{C}$  with a 1.6 W flexible amide heater wrapped on  
the battery pack. The sub-gondola is powered by a 24 Wh lithium ion battery pack that is charged with four  
2 W photovoltaic arrays. Ambient temperature and pressure measurements are made with a  
Thermodynamical SENSor (TSEN) supplied by LMD and designed for sampling in the UTLS (Hertzog et  
190 al., 2007). The TSEN used by FLOATS is the same configuration used with the RACHuTS instrument and  
a broader description can be found in Kalnajs *et al.* (2021). Previous measurements have shown the TSEN  
design to be effective at reducing solar radiative heating biases normally associated with high altitude  
measurements. TSEN has an accuracy and precision of  $0.25^{\circ}\text{C}$  during the day and  $0.1^{\circ}\text{C}$  at night (Hertzog  
et al., 2004). The TSEN temperature probe hangs  $\sim 1$  m below the EFU with small gauge  
195 Polytetrafluoroethylene (PTFE) coated wire to reduce the effect of radiant heating from the EFU surface



during daylight hours. The GPS measurements are made with a UBlox MAX-M8C module and have a specified position accuracy of 2.5 m. All engineering data, TSEN, and GPS data are collected every 10 s and transmitted via a Long Range (LoRa) radio module to the instrument gondola.

## 200 2.5 DTS Temperature Calibration

The conversion of the temperature dependent Raman backscattering per unit distance of the fiber optic cable to ambient temperature was adapted from the single ended DTS calibration methodologies provided in Hausner et al., 2011 and Suárez et al., 2011. In both methodologies, the temperature of a fiber optic cable can be estimated by (Suárez et al., 2011, Eq. 1):

205

$$T(z) = \frac{\gamma}{\ln [C] - \ln[R(z)] + \Delta\alpha z} \quad (1)$$

where  $T(z)$  is the temperature in K at the distance along the fiber  $z$  in meters,  $\gamma$  is the shift in energy between the incident laser wavelength and Raman scattering wavelength in K,  $C$  is a dimensionless calibration parameter,  $\Delta\alpha$  is the differential attenuation between the backscattered Stokes and anti-Stokes intensities, and  $R(z)$  is the measured ratio between the power of the Stokes backscattering to the anti-Stokes backscattering. To retrieve temperature,  $\gamma$ ,  $C$ , and  $\Delta\alpha$  must be known. Once  $\Delta\alpha$  is known for a given profile,  $\ln[C]$  can be estimated as follows (Suárez et al., 2011, Eq. 4):

210

215

$$\ln [C] = \frac{(\ln [R(z_1)] - \Delta\alpha z_1) T(z_1)}{T(z_1) - T(z_2)} - \frac{(\ln [R(z_2)] - \Delta\alpha z_2) T(z_2)}{T(z_1) - T(z_2)} \quad (2)$$

and  $\gamma$  can be estimated by (Suárez et al., 2011, Eq.5):

220

$$\gamma = (\ln [C] - \ln [R(z_1)] + \Delta\alpha z_1) T(z_1) \quad (3)$$

225

In both equations,  $z_i$  and  $z_j$  are points or sections of fiber optic cable at an externally measured uniform, but different, temperature. For FLOATS,  $T(z_i)$  and  $T(z_j)$  are the temperatures of RS1 and RS2, and are measured independently (Fig. 1b). These sections are held at different temperatures by actively heating RS1 to a set point of 30°C and allowing RS2 to passively heat to the internal gondola temperature, typically in the range of -30 – 30°C.



With the Hausner et al. (2011) methodology, the  $\Delta$  parameter of a DTS system can be independently calculated for each DTS profile by finding  $d\ln[R(z)]/dz$  from a section of the fiber optic cable at uniform temperature. In laboratory thermal chamber experiments the FLOATS reference sections were found to produce widely different  $\Delta\alpha$  compared to the sensing fiber optic possibly because of dissimilarity in fiber  
230 optic cable, or because of low temperature related effects like strain on the fiber optic and microbending loss (Hanson, 1979). The reference sections are therefore not reliable benchmarks for attenuation of the deployable fiber optic cable in the UTLS environment. Additionally, under an ideal DTS setup there would be no connections between components, hence zero loss. For FLOATS this is not possible and the fiber optic unions along the optical path of the DTS generate insertion loss, or step losses in Raman backscattering  
235 signal. Hausner et al. (2011) shows that step losses can be corrected by applying a linear offset to  $\ln[R(z)]$ , but this method likely assumes that the fiber optic union and  $\pm 0.5$  unit distance of the spatial resolution from the center of the union is at a uniform temperature. This is also not the case with FLOATS because the fiber optic unions are between reference components held at different temperatures, or optically undefinable sections like the spooled section of fiber. Optical unions in this orientation are required for integration of the  
240 optical components (i.e. reference sections and rotary joint) into the optical system and for assembly into the instrument gondola. Therefore, methods were developed to account for the temperature effects on  $\Delta\alpha$  and optical union step loss in the FLOATS system by a two-step optimization scheme. These methods are fully described in Appendix A, but are summarized here. First the step loss between the Reference Sections internal to the gondola for the experiment is found empirically as the difference in Raman backscattering between  
245 RS2 and RS1 when the temperature offset between the two sections is equal to  $0^\circ\text{C}$ . Second, the step loss between the remaining optical unions and  $\Delta\alpha$  for each profile is determined by minimizing the absolute mean bias between the calculated temperature and the independently observed temperature of each reference section as outlined in Hausner et al., (2011). By these methods the parameters required to calculate temperature using Eq. 1 (i.e.  $\gamma$ ,  $C$ , and  $\Delta\alpha$ ) can be determined dynamically for each profile within a given  
250 experiment.

## 2.6 Wyoming Test Flight

A validation flight of FLOATS was conducted on 22 January 2021 from Laramie, Wyoming ( $41.3^\circ$  N,  $105.7^\circ$  W; 2228 m above sea level) to test and characterize the instrument for the Stratéole 2 mission. The  
255 flight, named WY933, was aboard a 283 m<sup>3</sup> Raven Aerostar zero pressure vented balloon with a target constant altitude float level of 20 km. The flight launch time was 05:43 Local Time (LT). The flight train consisted of the balloon, a time and altitude controlled balloon cut away device, a secondary balloon cut away





device, a parachute, a strobe light, a time controlled parachute cutaway device, a radar transponder, and an instrument gondola. The instrument gondola was built of T-slotting framing rails with extruded polystyrene walls for insulation and approximated a Stratéole 2 gondola. Outside of the gondola was a GPS tracking device, and an iMet-1-RSB radiosonde (Fig 1a). The radiosonde provided high accuracy pressure, temperature, relative humidity, winds, and GPS position at the gondola flight level at a sampling rate of 1 second. The radiosonde telemetry was received by a mobile ground station. FLOATS was equipped with a 1200 m spool of fiber optic cable.

265

### 3 Results and Discussion

#### 3.1 WY933 Flight Summary

Figure 2 shows the instrument gondola GPS altitude and vertical distance between the gondola and EFU determined by the EFU GPS as a function of time for WY933. The fiber optic reel out started at 05:58 LT, 15 minutes after launch, at a GPS altitude of 5820 m. The reel out completed at approximately 06:30 LT with the complete deployment of 1167 m of fiber optic cable, based on optical length, at an altitude of 13600 m. The gondola reached its float altitude of 19140 m at 06:45 LT about 110 km down range from the launch site. The fiber optic remained fully deployed until 08:15 LT when automated fiber optic retraction began. The gondola was cut-away after drifting horizontally for nearly 90 km. All flight control times were designed to provide adequate time for ascent, fiber optic reeling, fully deployed temperature profiling and parachute descent while maintaining a radio communicable flight distance.

275

FLOATS retrieved a total of 381 DTS profiles with a sampling period of 20s and a deployment length greater than 8 m. The gondola crossed the tropopause at about 11 km with a temperature of  $-53^{\circ}\text{C}$ . At float altitude, the ambient temperature ranged from  $-62.6^{\circ}\text{C}$  to  $-54.8^{\circ}\text{C}$  with an average of  $-57.9^{\circ}\text{C}$  (Fig. 2). The iMet-1-RSB temperature, however, did report large spikes in temperature, at 07:15 and 08:30 LT for example, suggestive of the temperature sensor being in direct sunlight and poorly ventilated for short periods of the flight. Based on the gondola-altitude adjusted solar zenith angle (SZA) shown in Figure 2,  $\text{SZA} < 90^{\circ}$  were observed by the gondola at about 16 km or 06:40. The observed SZA less than  $90^{\circ}$  reveals that FLOATS was in some degree of direct sunlight for the entirety of time the fiber optic was fully deployed. Thus, the effect of solar radiative heating on the fiber optic cable and the resulting DTS temperature cannot be assessed from WY933. Solar radiative heating is a known concern for ground-based atmospheric DTS systems (de Jong et al., 2015), but ventilation by vertical wind shear along the length of the fiber optic cable will likely reduce the effect of solar heating on the FLOATS temperature profiles. Vertical wind shear and radiative heating will be addressed in the Stratéole 2 campaign where large daytime and nighttime datasets will be available.

285

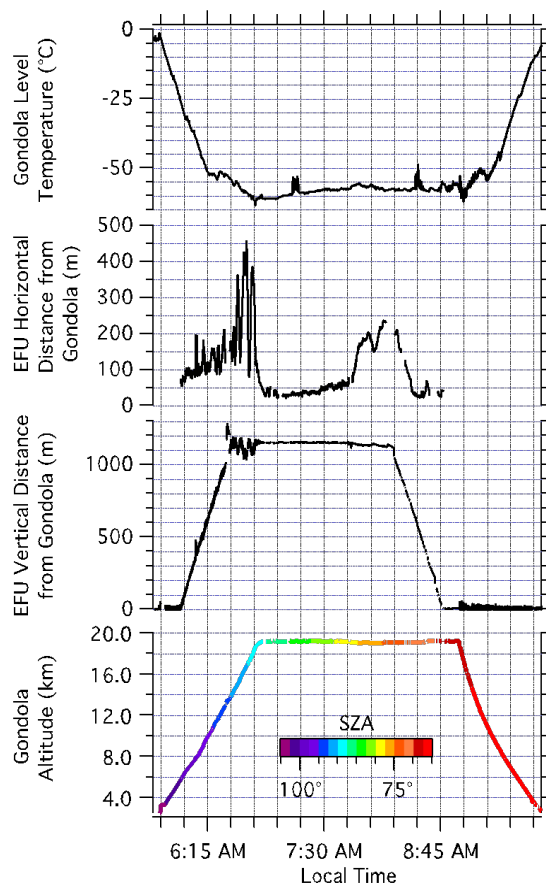


290

295

300

305



310

**Figure 2:** Summary of flight conditions of the 22 January 2021 WY933 zero pressure balloon flight. Altitude-adjusted solar zenith angle is displayed in rainbow.

Unfortunately, the EFU TSEN thermistor was damaged during the WY933 launch and was unable to report end of fiber temperature, although the position of the EFU was recorded. Because of the damaged sensor, modifications to the temperature calibration method discussed in Section 2.2 and Appendix A were made to retrieve temperature from the WY933 Raman backscattering profiles. These modifications are unique for the ascent/descent profiles and the float altitude profiles. For the ascent/descent profiles, RS4 temperature was derived from the iMet-1-RSB temperature profile by matching GPS altitudes from radiosonde and the EFU. For the float altitude profiles, a static attenuation parameter was estimated from the ascent profiles closest to the float level. The float level temperature profiles were then retrieved from a 3-

315



320 Reference Section calibration where only the rotary joint step loss value was optimized as discussed in Appendix A.

### 3.2 End of Fiber Position

325 The position of the end of the fiber is a useful tool to evaluate the position of any point along the fiber and thus the geospatial position of any FLOATS distributed temperature measurement. As seen in Figure 2 the end of fiber altitude relative to the instrument gondola altitude during WY933 is not constant even after the fiber optic is fully deployed. For example, the vertical distance between the gondola oscillated in the lower stratosphere before reaching float altitude. These oscillations are related to the horizontal offset between the instrument gondola and EFU estimated with the Haversine formula to calculate great circle  
330 distance. The EFU horizontal distance from the instrument gondola is given in Figure 2 and shows an inverse relationship to the vertical distance. Here the maximum horizontal distance was observed during the oscillation period prior to when float altitude is reached and then dampens to a minimum of 27 m at the start of the float altitude period. The horizontal separation increases with time during the float altitude period and reaches another maxima directly prior to the fiber optic reel in. The inverse relationship between the vertical  
335 and horizontal displacements of the end of fiber suggests that a right triangle model within a Cartesian plane may be used to describe or partially describe the position of the entire fiber relative to the gondola.

Using the right triangle model, by defining the hypotenuse as the shortest distance between the gondola and the EFU, the average distance between them while fully deployed was estimated to be  $1153 \pm 7$  m. Given the spatial inaccuracies of both GPS units and other uncertainties, the estimated orthogonal distance  
340 compares well with the 1167 m deploy distance estimated by DTS optical length. Therefore, there was likely little to no curvature in the deployed fiber optic cable during WY933 and the right triangle model can be used to evaluate the geospatial position of the FLOATS fiber optic. Curvature of the deployed fiber optic can lead to difficulties interpreting geospatial results and therefore should be flagged in any dataset. A case where the calculated hypotenuse is significantly shorter than the optical length of the fiber optic cable, would suggest  
345 that the fiber is exhibiting significant curvature resulting in increased uncertainty in the derived geometric altitude for positions along the fiber.

Figure 3a gives the three-dimensional translation of the end of fiber position by showing the position of the end of fiber in degrees from the nadir view of the gondola as a function of geographic bearing for the ascent and float altitude phase of flight. Over the course of the WY933 flight the end of fiber angle from  
350 nadir had an average value of  $6.7^\circ \pm 5.0^\circ$  with a range of  $1.0^\circ$  to  $29^\circ$ . The angles were observed during all periods of ascent and the fiber optic exhibited both pendulum and rotational patterns suggesting effects from



wind shear along the ascent path (Fig 3b), which will be explored further in Section. 4.5. After ascent, the rotational motions are dampened and the angle from nadir is reduced to less than  $10^\circ$  (Fig. 3a). For reference, a  $10^\circ$  offset from nadir produces a vertical displacement of about 1.5% at the end of the fiber compared to a nadir profile. The same degree of offset generates a horizontal displacement of about 17% compared to a nadir profile. The displacements may be corrected for by applying the right triangle model to estimate the altitude of all points along the fiber. However, the application of the model depends on the FLOATS dataset and minimum error needed for interpretation of those results. These above geospatial methods provide a framework that can be used to evaluate the quality of future FLOATS temperature profiles.

360

365

370

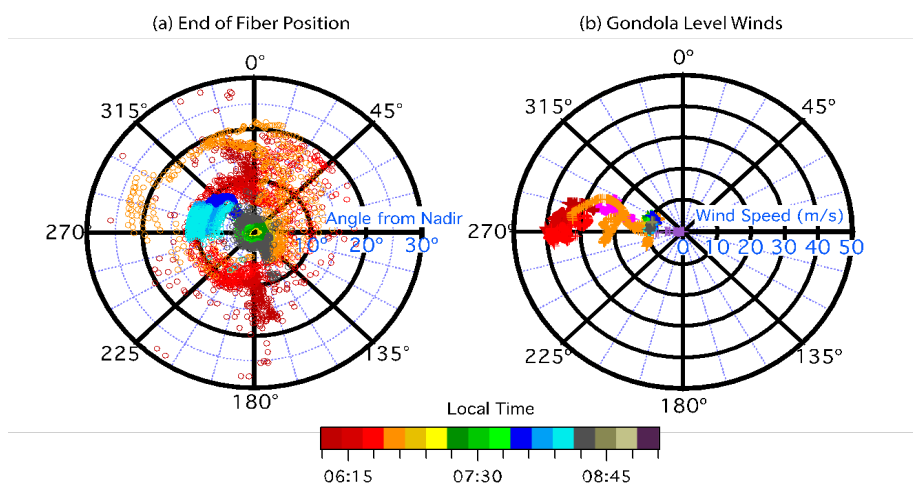


**Figure 3.** Polar graphs of (a) the end of fiber position angle in degrees with respect to nadir from the gondola and geographic bearing and (b) the wind speed in m/s and wind direction in degrees observed at the gondola level. Markers (rainbow) are colored by the local time (MST)

375

### 3.3 DTS Performance

The onboard reference temperature sensors (Fig. 1b) were used to evaluate the performance of the DTS temperature profiles from the ascent and float altitude of WY933. Since the EFU TSEN was damaged only the gondola level iMet-1-RSB temperature coincident to the EFU altitude could be used for the RS4 temperature during the ascent phase. The float altitude profiles were then calibrated using only the internal Reference Sections and RS3. For each reference section, every 1 meter point within that section was used to find the root mean square error compared to its respective sensor as follows:

380



$$RMSE = \sqrt{\frac{\sum_{i=1}^n (T_i - T_{ref})^2}{n}} \quad (4)$$

385

where  $T_i$  is the DTS temperature of a given point within a reference section with  $n$  observations, and  $T_{ref}$  is the reference section temperature.

The average RMSE for each reference section during ascent after the fiber optic was fully deployed, and at float altitude, are shown in Table 1. Generally, the error observed with the DTS observation in RS1 and RS2 were less than 0.3° C from all periods of flight and is representative of the minimum error in the measurement. The low error associated with these sections is likely because the sections are used to calculate the calibration parameters  $C$  and  $\Delta\alpha$  as shown in Eq. 2 and Eq. 3. Also, because the sections are close to the incident laser there is large signal to noise in the Raman backscattering. This is a known characteristic of DTS and the FTR3000 datasheet for example shows a 1.4° C difference in temperature accuracy between measurements at 500 m compared to 2000 m using the manufacturer's calibration. The ascent phase reference sections outside of the gondola were found to have RMSE of  $1.15 \pm 1.38^\circ\text{C}$  (RS3) and  $1.22 \pm 0.58^\circ\text{C}$  (RS4) respectively. The comparable RMSE observed with RS3 and RS4 and larger standard deviation observed with RS3 was unexpected and doesn't follow what is known about accuracy as a function of distance down the fiber. Similar RMSE was observed between all ascent profiles and those when the fiber optic was fully deployed. During float the DTS performed better than during ascent with an almost 75% decrease in error observed with RS3 (Table 1). The RMSE error for RS4, however, is unknown because of the damaged EFU TSEN. During the retraction period of the float altitude phase of flight the DTS at RS3 performed poorly with a two order of magnitude increase in RMSE.

Based on the error statistics from the reference sections there are several conclusions that can be applied to the interpretation of the temperature profiles as a whole. First, the Raman backscattering profiles from the fiber optic retraction period cannot be used for temperature retrievals. The reason for the large error observed during retraction is not fully understood, but is thought to be due to damage to the optical core of the fiber optic cable, temperature induced micro-bend losses, or a combination of both. The same error was not observed during the deployment phase, suggesting that the temperature of the fiber optic being spooled/unspooled may have an effect on optical losses. For reference, the WY933 reel was spooled in laboratory conditions and deployed at gondola temperatures greater than  $-10^\circ\text{C}$ , while the fiber was retracted at temperatures less than  $-55^\circ\text{C}$ . The effect of spooling/unspooling temperatures may also play a part in the increased RMSE observed with RS3 between the fully deployed ascent and fully deployed float altitude phases. The recently deployed fiber optic may not have reached full temperature stabilization outside of the



415 gondola within the 20 second sampling period and caused the observed differences between the reference  
 temperature and DTS temperature. The similar or greater RMSE observed with RS4 during ascent compared  
 to RS3 suggests that response time of the DTS may be slower than the change in ambient temperature during  
 ascent. This is a reasonable assumption because the average ascent rate of the balloon was 4.3 m/s and  
 therefore there was likely some vertical ‘smearing’ of the DTS temperature over 20 seconds.

420

**Table 1:** The average and standard deviation of the RMSE of the FLOATS DTS reference section  
 temperature compared to the reference temperature sensors for the ascent and float level profiles.

DTS Profile Type	Reference Section	RMSE ( $\mu \pm \sigma$ )
Ascent (116 profiles)	1	$0.29 \pm 0.04$
	2	$0.29 \pm 0.05$
	3	$1.15 \pm 1.38$
	4	$1.22 \pm 0.58$
Ascent – fully deployed (41 profiles)	1	$0.29 \pm 0.03$
	2	$0.27 \pm 0.05$
	3	$1.41 \pm 2.18$
	4	$1.30 \pm 0.69$
Float level – fully deployed (179 profiles)	1	$0.24 \pm 0.04$
	2	$0.26 \pm 0.04$
	3	$0.35 \pm 0.81$
Float level – fiber retraction (91 profiles)	1	$0.22 \pm 0.03$
	2	$0.24 \pm 0.04$
	3	$12.4 \pm 11.9$

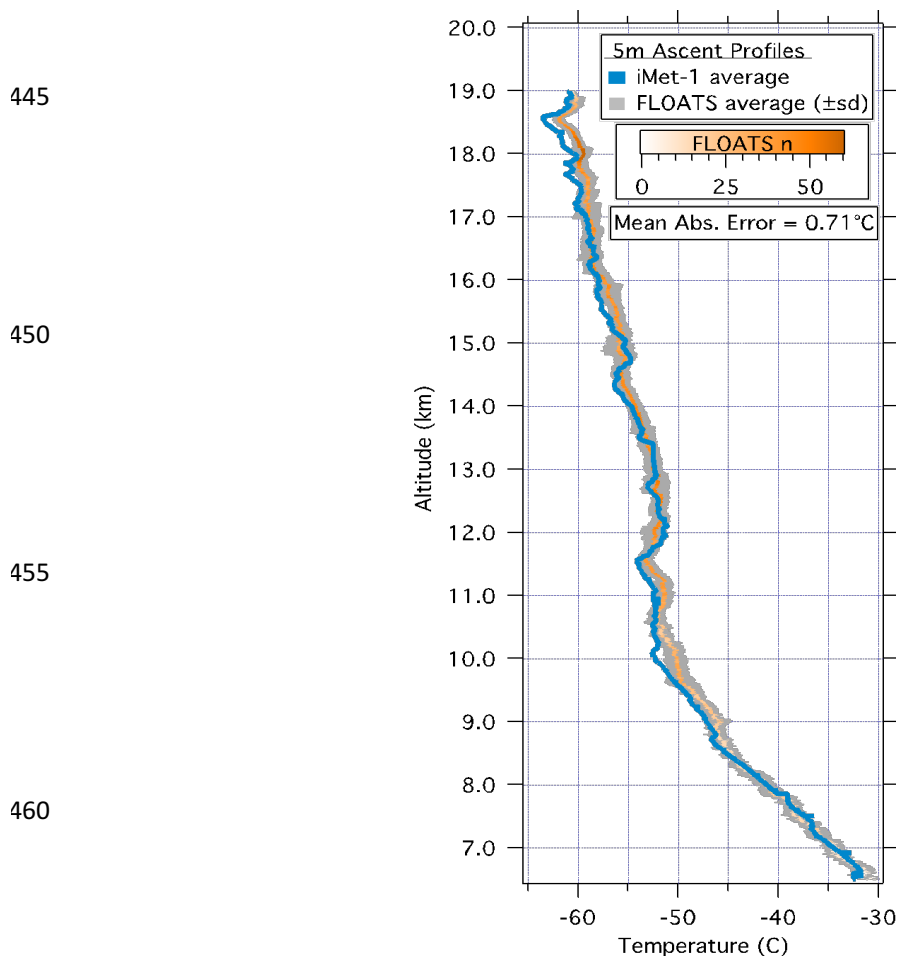
425 To further evaluate the performance of the FLOATS temperature profiles, full length ascent period  
 profiles are compared to the iMet-1-RSB aboard the instrument gondola. Figure 4 shows the FLOATS  
 temperature profiles averaged into 5 m altitude bins from 6.5 km to 19 km. The number of profile points  
 averaged into each bin presented in Figure 4 is colored by orange gradient on the trace showing that upwards  
 of 55 individual 1 m samples within each altitude bin were included in the ascent average. The standard  
 deviation, shown in grey, indicates that there was little variability in the DTS temperature at a single altitude  
 430 with an average standard deviation of  $0.9^\circ\text{C}$  and a range of  $0.3^\circ\text{C}$  to  $1.6^\circ\text{C}$  (Fig. 4). The FLOATS ascent  
 average compares well with the radiosonde altitude binned average at the same altitude and follows the same  
 vertical trends. However, there does appear to be decreased vertical resolution observed with the FLOATS  
 profiles corresponding to lower response to fast changes in the environmental lapse rate. This lower response



435 suggests that vertical ‘smearing’ due to a fast ascent rate compared to the DTS sampling period may be  
responsible. Using the mean absolute error (MAE) defined as:

$$MAE = \frac{\sum_{i=1}^n |T_{obs} - T_{avg}|}{n} \quad (5)$$

440 where  $T_{obs}$  is the average iMet temperature and  $T_{avg}$  is the average FLOATS for a given 5 m altitude bin  $i$ , and  
 $n$  is the number of altitude bins. The MAE was found to be  $0.71^\circ\text{C}$  for the DTS ascent profile compared to  
the reference temperature profile.





465 **Figure 4:** Ascent temperature profiles of the gondola level iMet radiosonde (blue line) and the DTS scans averaged into 5 meter bins. The DTS average temperature (orange gradient) is colored by the number (n) of 1m DTS sample points averaged for each 5 m bin. The standard deviation of the 5m DTS bins is shown in grey.

### 3.4 Float Level Temperatures

The 3-Reference Section calibrated temperatures at the WY933 float altitude can be seen in the curtain plot found in Figure 5a. In the figure FLOATS profile temperatures are displayed as a function of altitude and local time. At the start of float altitude, FLOATS records a relative flat temperature profile near  $-61^{\circ}\text{C}$  reaching from  $\sim 18\text{ km}$  to  $\sim 19.1\text{ km}$  with a cold band centered at  $18.5\text{ km}$ . This cold band was observed to have a minimum temperature of  $-63.0^{\circ}\text{C}$  and is consistent with the local cold-point temperature of  $-63.5^{\circ}\text{C}$  and thermal structure observed in the iMet-1-RSB ascent profile at the same altitude (Fig 5c). Looking at the first 2 minutes of FLOATS measurements at float altitude the average profile was found to have a MAE of  $1.0^{\circ}\text{C}$  compared to the iMet ascent profile. At about 06:55 to 07:05 LT the segment of profile at altitudes greater than  $18.55\text{ km}$  began to warm to temperatures between  $-59^{\circ}\text{C}$  and  $-60^{\circ}\text{C}$  and the lower altitudes in the profile remain at a consistent temperature with an average of  $-60.8^{\circ}\text{C}$  (Fig. 6a). Warming at the top half of the FLOATS fiber optic that wasn't observed at the bottom suggests that the instrument was entering a warm layer at those altitudes and that the warming trend wasn't due to solar heating of the cable even as the SZA reached  $85^{\circ}$  during that period (Fig. 6b). At 07:05 the layer between about  $18.5\text{ km}$  to  $19.1\text{ km}$  warmed to an average of  $-58.5^{\circ}\text{C}$  and the lower layer between about  $18.0\text{ km}$  and  $18.5\text{ km}$  warmed slightly to an average of  $-60.1^{\circ}\text{C}$ . This trend continued until 07:45 local time with an average of  $-57.8^{\circ}\text{C}$  in the upper altitude layer and an average of  $-59.8^{\circ}$  observed in the lower altitude layer between those time periods. The temperatures in the upper layer correspond well with the  $-57.6^{\circ}\text{C}$  average gondola level temperature reported from the iMet-1-RSB for the period between 07:15 to 07:45 (Fig. 6b). The period between 07:05 and 07:15 was excluded from the gondola level average to remove the assumed biasing due to solar radiative heating of the sensor. After this period a  $\sim 2^{\circ}\text{C}$  average warming was observed in the upper thermal layer from 07:45 to 08:15 and between  $18.40\text{ km}$  and  $19.1\text{ km}$  (Fig. 6a). Only a slight warming was observed for the lower altitude layer during that time with an average of  $-59.2^{\circ}\text{C}$ . As shown in Figure 5a, the fiber optic reel in begins at about 08:15 and after that period the FLOATS temperature profiles become inconsistent compared to the previous profiles probably because of optical distortion. Because of this distortion, the profiles from the reel in period are excluded from any analysis and comparison to the iMet-1-RSB descent profile. The reported descent profile, however, had similar thermal structure to the FLOATS profiles from the period prior to reel in (Fig. 5c). A narrow cold layer was seen at  $18.3\text{ km}$  and above  $18.4\text{ km}$  a  $\sim 700\text{ m}$  warm layer with





500 a maximum temperature of  $-52.9^{\circ}\text{C}$  was reported. A comparison of the average FLOATS temperature profile 2 minutes prior to reel in and the descent profile at the same altitude revealed a MAE of  $1.3^{\circ}\text{C}$ . By contrast the same FLOATS average had a MAE of  $4.0^{\circ}\text{C}$  compared to the iMet-1-RSB ascent profile. The overall agreement in thermal structure between the reported ascent and descent profiles and the FLOATS profiles demonstrate that FLOATS aboard a near constant altitude balloon is an effective tool for understanding the evolution of vertical structure at a high spatial and temporal resolution over a continuous domain.

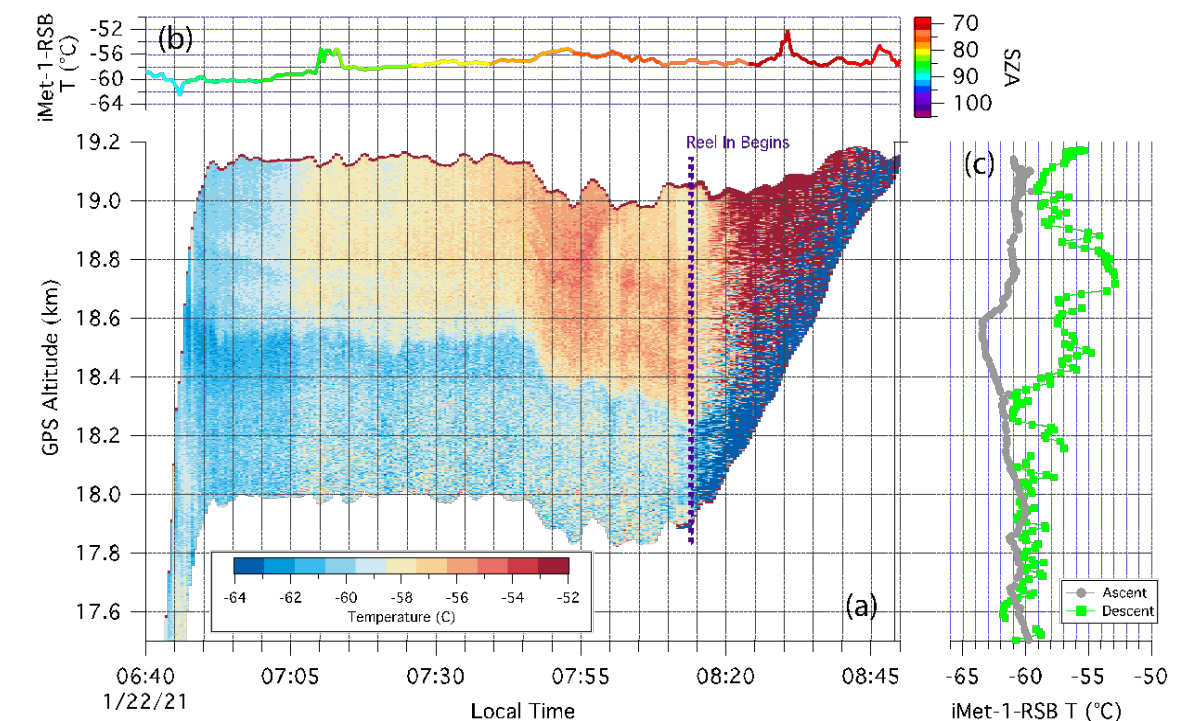


**Figure 5:** (a) Curtain plot of DTS profile temperatures in  $^{\circ}\text{C}$  at or near flight altitude as a function of altitude and local time. (b) Gondola level temperature in  $^{\circ}\text{C}$  as a function of local time and colored by the altitude adjusted solar zenith angle. (c) The gondola level ascent and descent temperature profiles in  $^{\circ}\text{C}$  as a function of altitude. The time where the fiber optic reel in begins is indicated with a dashed purple line.

### 505 3.5 Comparison with Outside Datasets

Temperature profiles from outside the WY933 flight including COSMIC-2 and local meteorological soundings are used to further evaluate the performance of FLOATS. Sounding data was retrieved from the Wyoming Upper Air website (<http://weather.uwyo.edu/upperair/sounding.html>) for the Denver, CO (DNR;



72468) and the Riverton, WY (RIW; 72672) stations for January 22, 2021 12 UTC. Level 2 AtmPrf  
510 COSMIC-2 temperature profiles for January 20, 2021 to January 24, 2021 were downloaded from the UCAR  
CDAAC website (<https://data.cosmic.ucar.edu/>). Because of the low inclination orbit of the COSMIC-2  
constellation and subsequent sparse spatial coverage at mid-latitudes only 58 profiles within a  $\pm 12^\circ$  longitude  
and  $\pm 6^\circ$  latitude range of WY933 were available for the 5-day period based on the perigee point of the radio  
occultation. Three COSMIC-2 profiles were within a 400 km radius of WY933 within 12 hours of the flight.  
515 A profile located at  $39.69^\circ$  N and  $106.82^\circ$  W at 13:00 LT was the closest matching COSMIC-2 profile to  
WY933. Following similar methods to (Alexander et al., 2008) the COSMIC-2 profiles were also used to  
generate a 5 day background temperature profile for a  $\pm 6^\circ$  longitude by  $\pm 3^\circ$  latitude grid box centered at  $104^\circ$   
W and  $40^\circ$  N. The average of the 21 COSMIC-2 profiles that fit the criteria were used as the background  
temperature profile for the study region.

520 The temperature profiles from the outside datasets and the FLOATS WY933 flight can be seen in  
Figure 6, where the geopotential altitudes have been converted to geometric altitude for comparison between  
the datasets. Generally, the FLOATS average ascent profile compared well with the sounding and best match  
COSMIC-2 profile. All datasets revealed similar broad thermal structure. A lapse rate tropopause at or near  
11 km, then a temperature inversion transitioning to a negative lapse rate up to about 17 km where there was  
525 a divergence in vertical structure. Error analysis between the FLOATS ascent profile and outside datasets  
produce a MAE of  $1.34^\circ\text{C}$  for the full altitude comparison between the FLOATS and COSMIC-2 best match,  
 $1.95^\circ\text{C}$  compared to the RIW sounding, and  $3.07^\circ\text{C}$  compared to the DNR sounding. Based on a MAE of  
 $3.23^\circ\text{C}$  between the RIW and DNR soundings the observed error between the FLOATS ascent profile and  
others is reasonable based on spatial and temporal differences between the datasets.

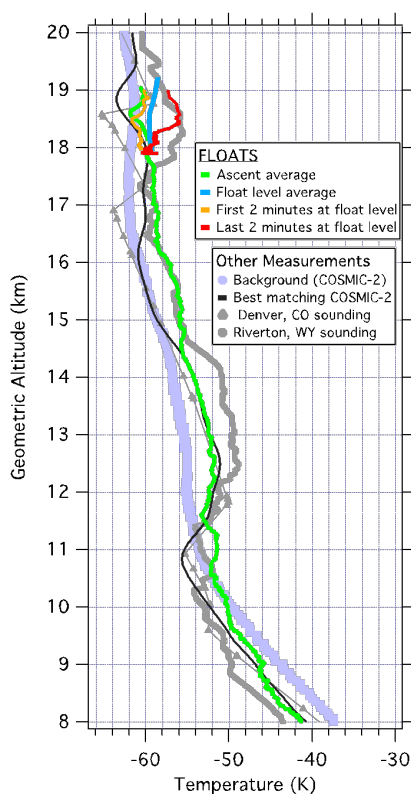
530 The FLOATS average temperature profile at float altitude also compared well to the outside datasets  
and is within a similar range of all observations (Fig 6.) Error analysis reported a MAE of  $2.40^\circ\text{C}$ ,  $2.79^\circ\text{C}$ ,  
and  $3.23^\circ\text{C}$  for the float level average compared to the COSMIC-2, RIW, and DNR profiles at the same  
altitude, respectively. The differences between the temperature profiles appear to be related to the FLOATS  
profile time. The average of the first two minutes from float altitude exhibits a vertical structure similar to  
535 the DNR profile with a cold layer near 18.5 km (Fig. 6). Whereas, the average of the last two minutes more  
closely matched the RIW profile with a warm layer centered at the same altitude. The coincident thermal  
structure and range of the temperature measurements further validates the FLOATS DTS profiles and  
provides additional evidence for limited biasing due to solar radiative heating of the fiber optic cable.

540 Finally, evaluation of the FLOATS DTS profiles compared to the COSMIC-2 background profile  
shows possible wave related variability in the profiles with altitude. As seen in Figure 6, the flight level



average suggests that WY933 was in an  $\sim 2^\circ$  C warm phase region compared to the COSMIC-2 average. Additionally, differences in the FLOATS profiles compared to COSMIC-2 were observed during different periods of flight. These comparisons suggest that FLOATS data can be used to evaluate wave driven temperature anomalies like those described in [Kim et al., 2016](#) and [Chang and L'Ecuyer, 2020](#) or to evaluate  
545 small scale energy states similar to methods described in Alexander et al. (2008).

550



555

560

565

**Figure 6:** Temperature profiles in  $^\circ\text{C}$  for the background temperature derived from COSMIC-2 temperature, radio sounding temperatures from Denver, CO (Station 72469) and Riverton, WY (72672) for 22 January 2021 12 UTC and FLOATS DTS. The FLOATS 5 m ascent profile (green), float level average (blue), and average temperature profiles from the beginning (orange) and end (red) of float altitude are displayed.

### 3.5 Temperature Anomalies and Wave Analysis

570

Here we analyze atmospheric waves present in FLOATS measurements. In this analysis, we will focus on two different parts of the flight: first during the balloon ascent when the EFU underwent a series of oscillations between 06:35 – 06:50 LT, and second at float altitude during the period between 07:05 – 08:10



LT when an upper level warm layer was observed and the balloon float level dropped vertically by  $\sim 100$  m (Fig. 5a). To provide context for the wave anomalies in the FLOATS WY933 test flight, we use the twice-daily radiosonde profiles at Riverton, WY (RIW), which include  $T$  as well as zonal ( $u$ ) and meridional ( $v$ ) wind profiles. We choose a 3-day mean of these profiles to define a background that is subtracted, leaving higher frequency, subsynoptic anomalies. The RIW sounding closest in time at 12 UTC 22 January 2021 (Fig. 7a) shows stratospheric wind anomalies ( $u', v'$ ) varying with a 3-km vertical wavelength ( $2\pi/m$ ), and with  $v'$  phase leading  $u'$  in altitude. These are characteristic of an upward propagating inertia-gravity wave signal. Hodograph analysis (Hirota and Niki, 1985) of the ( $u', v'$ ) signals suggests this is a northeastward propagating inertia-gravity wave with intrinsic frequency ( $\omega$ ) of about  $1.5f$  (where  $f$  is the Coriolis frequency), or a wave period of  $\sim 11$ -12 hours. The gravity wave dispersion relation  $k^2 = (\omega - f)^2 m^2 / N^2$  can then be used to estimate the horizontal wavelength ( $2\pi/k$ ) of  $\sim 600$  km. The wind anomalies therefore suggest a slow and large-scale wave that is likely present in both the Riverton, WY radiosonde as well as the WY933 balloon ascent and FLOATS profiles.

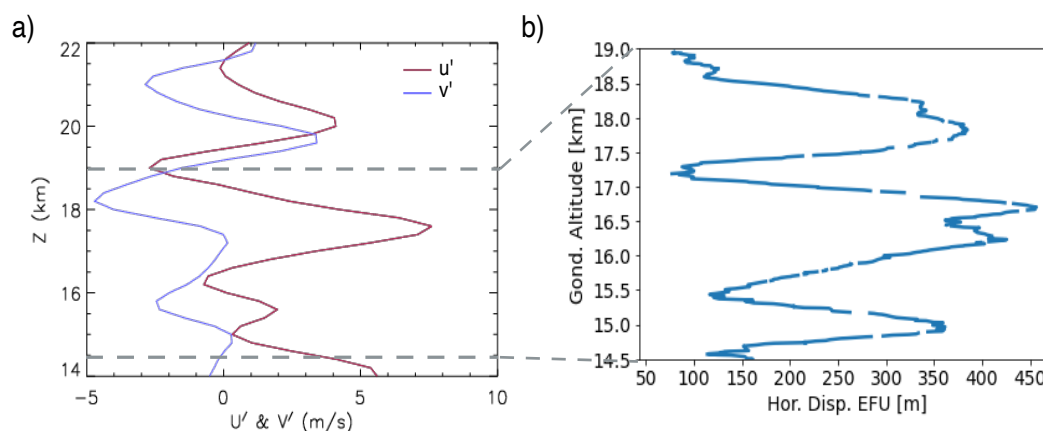


**Figure 7:** a) Meridional and Zonal wind perturbations as a function of altitude from radiosonde observations in Riverton, WY. b) Horizontal displacement of FLOATS EFU as function of gondola altitude.

FLOATS temperature perturbations,  $T'$ , were calculated throughout the flight as the difference between the 3-day mean  $T$  from RIW and the FLOATS profile temperature. Using FLOATS data binned to 1 minute temporal resolution and 200 m vertical resolution to match the vertical resolution of the RIW radiosonde observations.



During the ascent phase of WY933 the horizontal displacement of the EFU, at the end of the 1200 m fiber length, exhibits three distinct peaks between  $\sim 15$  km – 19 km (Fig. 7b). In the context of the WY933 balloon and EFU rising through the 3 km vertical wavelength inertia-gravity wave oscillations, the peaks in the horizontal EFU displacement would occur when the wind difference between the gondola and EFU is largest. This will occur once every half cycle of the inertia-gravity wave, resulting in three peaks in EFU displacement as the balloon rises the 4.5 km distance from 14.5 to 19 km. Therefore, we hypothesize that the oscillations of the EFU position are due to the vertical shear in the inertia gravity wave. FLOATS measured  $T'$  during ascent (Fig. 8a) show a warmer layer below 17 km followed by a cooler layer above 17 km. Riverton, WY sonde temperatures (Fig. 6) showed similar  $\pm 2$ °C temperature variations but with a different phase, cool below 17.5 km and warmer above. This is consistent with the interpretation that the same large-scale inertia-gravity wave is modulating  $T$  in both locations, but the phase varies over the  $\sim 300$  km distance between the two sites.

The second period of interest of the wave analysis is characterized by an increase in temperature starting at about 07:05 followed a further increase in temperature at 07:40 at an altitude range of 18.4 km to 19.1 km (Fig. 5 and 8a). To determine if the warming layer is related to higher frequency gravity wave activity, spectral analysis using the S-transform was conducted on the  $T'$  profiles (Stockwell et al., 1996), which decomposes the data in time-frequency space similar to a wavelet transform. The spectral analysis (Fig. 8b) shows enhanced spectral power  $> 0.4$  °C for wave period of about 55 min and 20 min. This suggests the increase in temperature at 07:05 LT can be related with the warm phase of gravity wave with a period of 55 minutes and the further increase in temperature at  $\sim 07:40$  LT related to a superposition of the 55 minute period gravity wave and a gravity wave with a period of 20 minutes.

This analysis shows the capabilities of FLOATS to detect a variety of gravity waves with differing spatial and temporal scales. As the float time during the test flight was limited to about 2 h the inertia gravity wave with a period of 8 h could not be fully sampled by FLOATS. However, in future long duration flights up to several months (Haase et al. 2018), the ability of FLOATS to sample small vertical and temporal scale structures will become valuable to observe both small- and large-scale waves, extending to global horizontal scales, while fully resolving very short vertical wavelengths that have important effects on cirrus clouds and global circulation (Bramberger et al., 2022), but are difficult to observe from other measurement platforms.



620

625

630

635

640

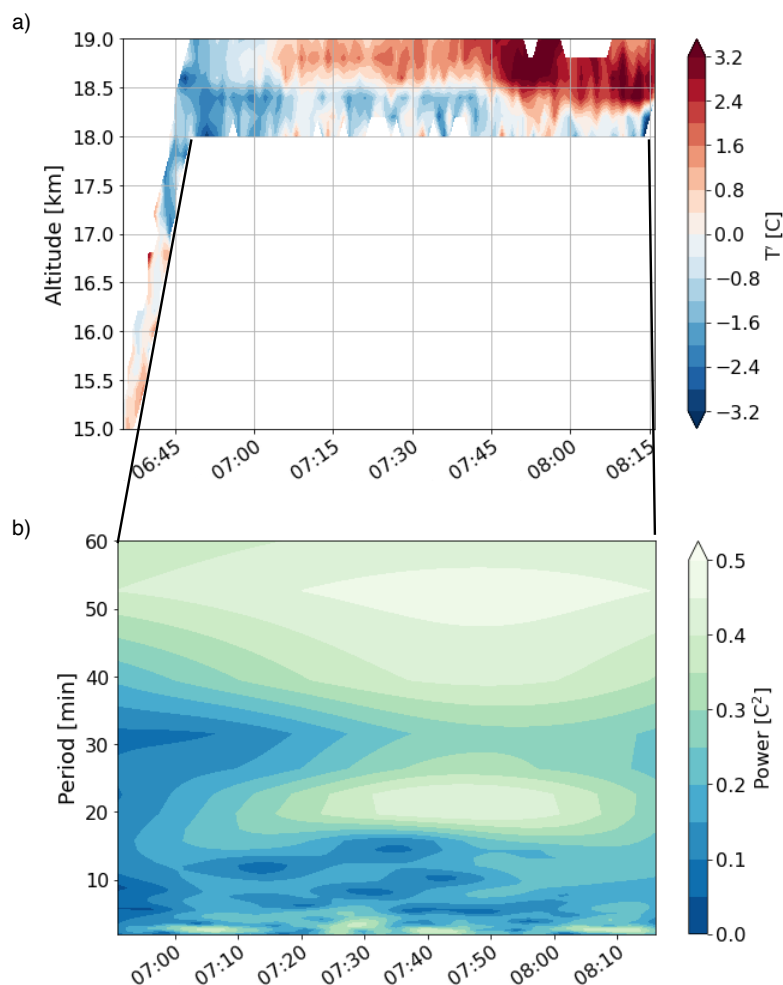


**Figure 8:** a) Temperature perturbations from FLOATS observed temperature as a function of altitude and local time. b) Spectral power from FLOATS temperature perturbations as a function of wave period and local time, for float level data only.

#### 4 Conclusions

Fiber optic distributed temperature sensing is an under-utilized tool for atmospheric measurements that provides low-cost and good performance temperature measurements at spatial and temporal resolutions not possible with other sensing methods. In the tropical tropopause layer, there is a need for enhanced temperature monitoring to address questions related to vertical transport of material and atmospheric wave propagation within the region. FLOATS is a DTS system designed for up to 2 km vertical temperature profiling in the UTLS aboard drifting constant altitude balloons with a minimum sampling period of 20 s and



650 a vertical resolution of 3 m. The instrument employs a mechanical reeling system, a self-contained end of fiber sub-gondola, and a 4-reference temperature optical system all designed for long duration use within the harsh conditions of the TTL.

An experiment with the system was conducted aboard a short duration vented balloon flight from Laramie, Wyoming, to validate FLOATS for the Stratéole 2 mission within the TTL. A major motivation for  
655 the 19 km altitude flight was to understand the technical performance of the 4-reference section calibration procedure with the fiber optic under stress loads and temperatures typical for the UTLS. Although the end of fiber temperature reference was damaged during launch an adapted 4-reference calibration was validated using the gondola level temperature sensor and produced RMSE values of  $\leq 1.4^\circ\text{C}$  for DTS temperatures compared to the ambient temperature sensor during the ascent phase of flight. These values show good  
660 confidence in the FLOATS measurements considering the DTS sampling was integrated over 20 s during the  $\sim 4\text{ m/s}$  ascent, and by producing an error of only  $0.71^\circ\text{C}$  compared to the gondola level temperature sensor. Evaluation with outside datasets, nearby radios soundings and COSMIC2 measurements, demonstrate similar confidence in the FLOATS measurements. The FLOATS ascent profile was within the range of temperature profiles observed by these other platforms. Float level temperature profiles from the validation flight  
665 demonstrate the ability of FLOATS to characterize small scale atmospheric dynamics like gravity waves, and larger scale dynamics like inertial gravity waves at a resolution not possible with other sensing platforms. This study establishes fiber optic distributed temperature sensing as a viable atmospheric measurement platform and FLOATS as a capable and unique balloon-borne temperature sensor for the UTLS.

## 670 **5 Appendix A – Temperature Retrieval Optimization**

To retrieve DTS temperature from the thermally complex setup of FLOATS a two-step optimization processing scheme was developed. The method is illustrated in Figure A1, which shows the Raman backscattering ratio as a function of optical distance along the fiber optic cable for a FLOATS profile from  
675 the mid-latitude flight described in Sect. 2.5 of the main text. First, the step losses due to the optical unions A and B (Fig. A1), that are positioned between Reference Section 1 (RS1) and Reference Section 2 (RS2), are assumed to be static but unique for each flight configuration. The step loss between the Sections are then estimated by finding the linear fit of  $(\ln[R(z_2)] + \Delta\alpha_{12}) - (\ln[R(z_1)] + \Delta\alpha_{12})$  vs  $T(z_2) - T(z_1)$  of all DTS measurements for the flight where  $z_1$  furthest point of RS1 and  $z_2$  is the nearest point of RS2 with respect to  
680 optical bench, or the nearest points to the connector, and  $\Delta\alpha_{12}$  is the average attenuation of the two reference sections derived from the slope of  $\ln[R(z)]$  as a function of distance for the two sections. The linear fit of step loss plot can then be used to extrapolate the step loss value for when the two Sections and optical unions are





at the same temperature (i.e.  $T(z_i) - T(z_j) = 0^\circ \text{C}$ ). An example of the linear fit and plotting method can be found in the supporting information Figure A2. If  $T(z_i) - T(z_j)$  is equal to  $0^\circ \text{C}$  during a flight then the  $(\ln[R(z_i)] + \Delta\alpha_{i2}) - (\ln[R(z_j)] + \Delta\alpha_{j2})$  from those times can be used as the primary method to retrieve the static step loss value of union A and union B for that flight, or as check of the linear extrapolation method described above. The applied step loss correction for union A and union B can be seen in Figure A1 as the light blue  $\ln(R)$  trace.

The step loss due to the fiber optic rotary joint is more difficult to determine because that region of the instrument contains the rotary joint union, varying lengths of spooled fiber optic cable during flight (which have uncertain micro bend and macro bend losses), and a large temperature transition from inside of the instrument gondola to the ambient air outside the gondola (e.g.  $\Delta T > 55^\circ \text{C}$  in the tropics). In Figure A1 this region of the Raman backscattering profile can be seen between the approximate optical distances of 65 m to 110m. The second step in the processing scheme is therefore to estimate the step loss due to the rotary joint and  $\Delta\alpha$  based on a four-reference section optimization. Here we use the optimization scheme discussed in Hausner et al. (2011) Eq. 7 for each 20 s temperature profile, by minimizing the absolute mean bias (MB):

$$MB = \frac{1}{mn} |\sum_1^m \sum_1^n (T_{DTS} - T_{obs})| \quad (1A)$$

where  $m$  is the number of reference sections,  $n$  is the number of DTS observations within the reference section,  $T_{DTS}$  is the temperature at that observation point, and  $T_{obs}$  is the externally observed temperature for that reference section. To perform the optimization,  $\Delta\alpha$  and the rotary joint step loss value (unitless) are parameterized into a range of  $0.0 \text{ m}^{-1}$  to  $1.98\text{e}^6 \text{ m}^{-1}$  and  $-9.0\text{e}^5$  to  $2.0\text{e}^3$ . The  $T_{DTS}$  is then calculated for each point along the reference section by solving for  $T(z)$  in Eq. 1 and by using Eq. 2 and Eq. 3. The  $T_{obs}$  for RS3 uses the first 10 m of fiber optic cable outside of the gondola and  $T_{obs}$  for RS4 uses the 10 m of fiber optic closest to the EFU (Fig. 1b and Fig A1). The  $T_{obs}$  for RS3 is obtained from a temperature sensor outside of the gondola. The  $T_{obs}$  for RS4 is obtained from the EFU TSEN. An example of an optimized Raman backscattering profile and approximate calibrated temperature can be seen as the purple trace in Figure A1. The benefit of the described dynamic calibration scheme with parameter optimization compared to the use of static parameters is that it accounts for real time changes of the backscattering signal due to strain effects, degradation of the incident laser, or other signal aberrations that could occur during a long duration ballooning mission like Stratéole 2.



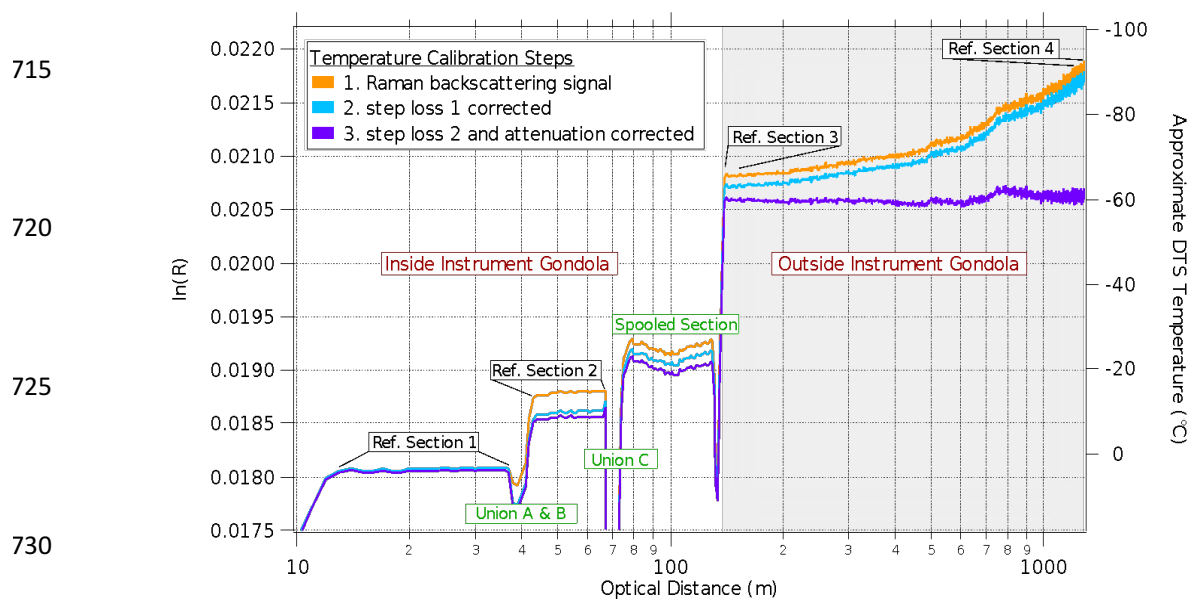
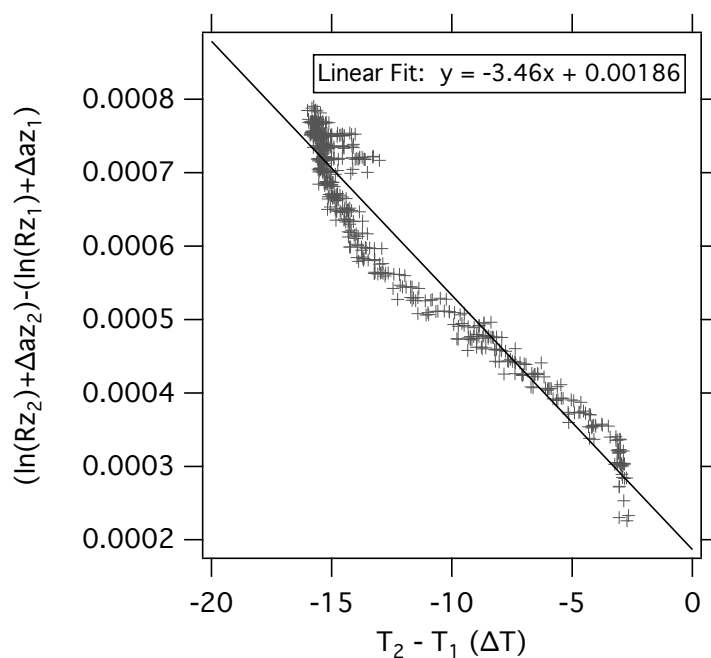


**Figure A1:** Raman backscattering ratio (left axis) and approximate DTS temperature (right axis) versus optical distance of FLOATS from an example profile with the full deployment of 1167 m of fiber. The raw back scattering signal (orange trace), step loss 1 corrected (blue trace), and optimized back scattering signal (purple trace) are shown. Locations of the uniform temperature reference sections are depicted with black boxes. Insertion loss and unsolvable sections are highlighted with green boxes.





765 **Figure A2:** The difference in processed Raman backscattering signal between Reference  
Section 1 and Reference Section 2 from the WY933 flight versus the difference in  
temperature between those sections (grey crosses). The linear fit of the data is shown as a  
black line.

## 6 Author Contributions

DG designed and built the instrument, led laboratory testing, and drafted this manuscript. Early  
development and conceptualization of the instrument was completed by LK, SD, and JA. The validation  
770 experiment was led by DG and LK, and the Wyoming balloon flight was headed by TD. The gravity wave  
analysis was conducted by MB and JA. All authors contributed to manuscript editing and revisions.

## 7 Data Availability

The data is available upon request from the corresponding author.

775

## 8 Competing Interests

The authors declare that they have no conflict of interest.

## 9 Acknowledgements

780 We would like to thank Dr. Matt Norgren for his assistance with the Wyoming test flight. We  
acknowledge funding support from the National Science Foundation under awards 1642277, 1642246 and  
1642644.

## 10 References

785

Alexander, S. P., Tsuda, T., Kawatani, Y., and Takahashi, M.: Global distribution of atmospheric waves in  
the equatorial upper troposphere and lower stratosphere: COSMIC observations of wave mean flow  
interactions, 113, <https://doi.org/10.1029/2008JD010039>, 2008.

790 Bramberger, M., Alexander, M. J., Davis, S., Podglajen, A., Hertzog, A., Kalnajs, L., Deshler, T., Goetz, J.  
D., and Khaykin, S.: First Super-Pressure Balloon-Borne Fine-Vertical-Scale Profiles in the Upper TTL:  
Impacts of Atmospheric Waves on Cirrus Clouds and the QBO, 49, e2021GL097596,  
<https://doi.org/10.1029/2021GL097596>, 2022.

795 Chang, K.-W. and L'Ecuyer, T.: Influence of gravity wave temperature anomalies and their vertical  
gradients on cirrus clouds in the tropical tropopause layer – a satellite-based view, 20, 12499–12514,  
<https://doi.org/10.5194/acp-20-12499-2020>, 2020.

Drusová, S., Bakx, W., Doornenbal, P. J., Wagterveld, R. M., Bense, V. F., and Offerhaus, H. L.:  
Comparison of three types of fiber optic sensors for temperature monitoring in a groundwater flow  
simulator, *Sensors and Actuators A: Physical*, 112682, <https://doi.org/10.1016/j.sna.2021.112682>, 2021.



- 800 Egerer, U., Gottschalk, M., Siebert, H., Ehrlich, A., and Wendisch, M.: The new BELUGA setup for collocated turbulence and radiation measurements using a tethered balloon: first applications in the cloudy Arctic boundary layer, 12, 4019–4038, <https://doi.org/10.5194/amt-12-4019-2019>, 2019.
- Fueglistaler, S., Dessler, A. E., Dunkerton, T. J., Folkins, I., Fu, Q., and Mote, P. W.: Tropical tropopause layer, 47, <https://doi.org/10.1029/2008RG000267>, 2009.
- 805 Haase, J. S., Alexander, M. J., Hertzog, A., Kalnajs, L. E., Deshler, T., Davis, S. M., Plougonven, R., Cocquerez, P., and Venel, S.: Around the World in 84 Days, 99, 2018.
- Hausner, M. B., Suárez, F., Glander, K. E., Giesen, N. van de, Selker, J. S., and Tyler, S. W.: Calibrating Single-Ended Fiber-Optic Raman Spectra Distributed Temperature Sensing Data, 11, 10859–10879, <https://doi.org/10.3390/s111110859>, 2011.
- 810 Henniges, J. and Masoudi, A.: Fiber-Optic Sensing in Geophysics, Temperature Measurements, in: Encyclopedia of Solid Earth Geophysics, edited by: Gupta, H. K., Springer International Publishing, Cham, 384–394, [https://doi.org/10.1007/978-3-030-58631-7\\_281](https://doi.org/10.1007/978-3-030-58631-7_281), 2021.
- Higgins, C. W., Wing, M. G., Kelley, J., Sayde, C., Burnett, J., and Holmes, H. A.: A high resolution measurement of the morning ABL transition using distributed temperature sensing and an unmanned aircraft system, *Environ Fluid Mech*, 18, 683–693, <https://doi.org/10.1007/s10652-017-9569-1>, 2018.
- 815 Hirota, I. and Niki, T.: A Statistical Study of Inertia-Gravity Waves in the Middle Atmosphere, 63, 1055–1066, [https://doi.org/10.2151/jmsj1965.63.6\\_1055](https://doi.org/10.2151/jmsj1965.63.6_1055), 1985.
- de Jong, S. a. P., Slingerland, J. D., and van de Giesen, N. C.: Fiber optic distributed temperature sensing for the determination of air temperature, 8, 335–339, <https://doi.org/10.5194/amt-8-335-2015>, 2015.
- 820 Kalnajs, L. E., Davis, S. M., Goetz, J. D., Deshler, T., Khaykin, S., St. Clair, A., Hertzog, A., Bordereau, J., and Lykov, A.: A reel-down instrument system for profile measurements of water vapor, temperature, clouds, and aerosol beneath constant-altitude scientific balloons, *Atmos. Meas. Tech.*, 14, 2635–2648, <https://doi.org/10.5194/amt-14-2635-2021>, 2021.
- 825 Keller, C. A., Huwald, H., Vollmer, M. K., Wenger, A., Hill, M., Parlange, M. B., and Reimann, S.: Atmospheric Measurement Techniques Fiber optic distributed temperature sensing for the determination of the nocturnal atmospheric boundary layer height, 4, 143–149, <https://doi.org/10.5194/amt-4-143-2011>, 2011.
- 830 Khaykin, S. M., Funatsu, B. M., Hauchecorne, A., Godin-Beekmann, S., Claud, C., Keckhut, P., Pazmino, A., Gleisner, H., Nielsen, J. K., Syndergaard, S., and Lauritsen, K. B.: Postmillennium changes in stratospheric temperature consistently resolved by GPS radio occultation and AMSU observations, 44, 7510–7518, <https://doi.org/10.1002/2017GL074353>, 2017.
- Kim, J.-E., Alexander, M. J., Bui, T. P., Dean-Day, J. M., Lawson, R. P., Woods, S., Hlavka, D., Pfister, L., and Jensen, E. J.: Ubiquitous influence of waves on tropical high cirrus clouds, 43, 5895–5901, <https://doi.org/10.1002/2016GL069293>, 2016.
- 835 Lagos, M., Serna, J. L., Muñoz, J. F., and Suárez, F.: Challenges in determining soil moisture and evaporation fluxes using distributed temperature sensing methods, *Journal of Environmental Management*, 261, 110232, <https://doi.org/10.1016/j.jenvman.2020.110232>, 2020.



- Lu, P., Lalam, N., Badar, M., Liu, B., Chorpene, B. T., Buric, M. P., and Ohodnicki, P. R.: Distributed optical fiber sensing: Review and perspective, *Applied Physics Reviews*, 6, 041302, <https://doi.org/10.1063/1.5113955>, 2019.
- 840 Peltola, O., Lapo, K., Martinkauppi, I., O'Connor, E., Thomas, C. K., and Vesala, T.: Suitability of fibre-optic distributed temperature sensing for revealing mixing processes and higher-order moments at the forest–air interface, 14, 2409–2427, <https://doi.org/10.5194/amt-14-2409-2021>, 2021.
- Petrides, A. C., Huff, J., Arik, A., Giesen, N. van de, Kennedy, A. M., Thomas, C. K., and Selker, J. S.: Shade estimation over streams using distributed temperature sensing, 47, <https://doi.org/10.1029/2010WR009482>, 2011.
- 845 van Ramshorst, J. G. V., Coenders-Gerrits, M., Schilperoort, B., van de Wiel, B. J. H., Izett, J. G., Selker, J. S., Higgins, C. W., Savenije, H. H. G., and van de Giesen, N. C.: Revisiting wind speed measurements using actively heated fiber optics: a wind tunnel study, 13, 5423–5439, <https://doi.org/10.5194/amt-13-5423-2020>, 2020.
- 850 Randel, W. J. and Jensen, E. J.: Physical processes in the tropical tropopause layer and their roles in a changing climate, *Nature Geosci*, 6, 169–176, <https://doi.org/10.1038/ngeo1733>, 2013.
- Sayde, C., Thomas, C. K., Wagner, J., and Selker, J.: High-resolution wind speed measurements using actively heated fiber optics, 42, 10,064–10,073, <https://doi.org/10.1002/2015GL066729>, 2015.
- Selker, J. S., Thévenaz, L., Huwald, H., Mallet, A., Luxemburg, W., Giesen, N. van de, Stejskal, M., Zeman, J., Westhoff, M., and Parlange, M. B.: Distributed fiber-optic temperature sensing for hydrologic systems, 42, <https://doi.org/10.1029/2006WR005326>, 2006.
- 855 Sinnett, G., Davis, K. A., Lucas, A. J., Giddings, S. N., Reid, E., Harvey, M. E., and Stokes, I.: Distributed Temperature Sensing for Oceanographic Applications, 37, 1987–1997, <https://doi.org/10.1175/JTECH-D-20-0066.1>, 2020.
- 860 Stockwell, R. G., Mansinha, L., and Lowe, R. P.: Localization of the complex spectrum: the S transform, 44, 998–1001, <https://doi.org/10.1109/78.492555>, 1996.
- Suárez, F., Aravena, J. E., Hausner, M. B., Childress, A. E., and Tyler, S. W.: Assessment of a vertical high-resolution distributed-temperature-sensing system in a shallow thermohaline environment, 15, 1081–1093, <https://doi.org/10.5194/hess-15-1081-2011>, 2011.
- 865 Thomas, C. K., Kennedy, A. M., Selker, J. S., Moretti, A., Schroth, M. H., Smoot, A. R., Tufillaro, N. B., and Zeeman, M. J.: High-Resolution Fibre-Optic Temperature Sensing: A New Tool to Study the Two-Dimensional Structure of Atmospheric Surface-Layer Flow, *Boundary-Layer Meteorol*, 142, 177–192, <https://doi.org/10.1007/s10546-011-9672-7>, 2012.
- 870 Tyler, S. W., Selker, J. S., Hausner, M. B., Hatch, C. E., Torgersen, T., Thodal, C. E., and Schladow, S. G.: Environmental temperature sensing using Raman spectra DTS fiber-optic methods, 45, <https://doi.org/10.1029/2008WR007052>, 2009.
- Zeidler, G., Hasselberg, A., and Schicketanz, D.: Effects of mechanically induced periodic bends on the optical loss of glass fibres, 18, 553–555, [https://doi.org/10.1016/0030-4018\(76\)90319-9](https://doi.org/10.1016/0030-4018(76)90319-9), 1976.